EES Solar

ROYAL SOCIETY OF CHEMISTRY

PAPER

View Article Online
View Journal | View Issue

Check for updates

Cite this: *EES Sol.*, 2025, **1**, 828

Hot carrier dynamics in operational metal halide perovskite solar cells

Hadi Afshari, *[a] Varun Mapara,[a] Shashi Sourabh,[a] Megh N. Khanal, [b]
Vincent R. Whiteside, [b] Rebecca A. Scheidt,[c] Matthew C. Beard, [c]
Giles E. Eperon,[d] Ian R. Sellers[b] and Madalina Furis[a]

Received 23rd April 2025
Accepted 15th July 2025

DOI: 10.1039/d5el00063g

rsc.li/EESSolar

One of the main approaches for inhibiting carrier cooling in semiconductor systems enabling the study of hot carrier solar cell protocols is the use of concentrated illumination to obtain high power densities and create a phonon bottleneck. This, however, typically also increases the lattice temperature of the solar cells significantly. Accordingly, solar cells subjected to high concentration illumination also need to withstand high operating temperatures. Having previously demonstrated the high temperature tolerance of triple halide perovskite ($FA_{0.8}Cs_{0.2}Pb_{1.02}I_{2.4}Br_{0.6}Cl_{0.02}$) solar cells, here the hot carrier relaxation dynamics are studied in these devices using high power transient absorption (TA) measurements. In addition to monitoring TA spectra obtained at different time delays, the thermalization mechanism of hot carriers is mapped with power dependent TA to extract the carrier cooling time in this system under *in operando* conditions and various bias conditions that reflect the J_{sc}, V_{max}, and V_{oc} of these structures, and subsequently deconvolve the underlying physics of carrier relaxation, as well as track the dynamics of thermalization close to working conditions of the solar cells. These measurements uncover a complex interaction of hot carrier thermalization involving temporal carrier density, transport, extraction, and apparent non-equivalent contributions with respect to non-equilibrium photogenerated electrons and holes in these metal halide perovskite solar cell architectures.

Broader context

Historically, the application of solar cell technology started in space to power satellites. But today one of the main missions for solar cell research is the pursuit of sustainable and renewable energy sources to mitigate climate change by transitioning away from fossil fuels, aiming to achieve carbon neutrality through efficient conversion of sunlight into electricity, while also considering factors like cost-effectiveness, grid integration, and environmental impact throughout the solar energy production lifecycle. The primary work to maximize the utilization of the Sun's energy lies in addressing the largest loss mechanisms within solar cells, notably thermalization and transmission losses. Thermalization occurs when high-energy photons are absorbed by the solar cell, creating high energy carriers that thermalize to the band edges. This process results in the biggest loss in solar cells: approximately 35% of the solar spectrum is wasted due to thermalization. Hot carrier solar cell architectures aim to increase the intra-band relaxation time of photogenerated carriers to values close to the carrier extraction time, such that carriers retain their kinetic energy upon collection, so that thermalization loss is minimized. Significantly, if achieved, such hot carrier solar cells promise power conversion efficiencies close to 60% for single junction solar cells.

Introduction

Historically, the application of solar cell technology started in space to power satellites.[1,2] Today, however, solar panels have become ubiquitous and come in many different forms, finding applications beyond conventional rooftop and utility solar installations, such as agrivoltaics, where the dual utilization of land for agriculture and solar farming proves lucrative for investors while conserving water through a substantial reduction in irrigation.[3,4] The new generation of electric vehicles incorporates solar roofs, capable of generating extra driving miles exclusively from sunlight, particularly advantageous in sunny cities.[5–7] Despite these advancements, the full potential of solar cell technology is yet to be realized.

The primary work to maximize the utilization of the Sun's energy lies in addressing the largest loss mechanisms within solar cells, notably thermalization and transmission losses.[8,9]

Thermalization occurs when high-energy photons are absorbed by the solar cell, creating high energy carriers that thermalize to the band edges.[8] This process results in the biggest loss in solar cells: approximately 35% of the solar spectrum is wasted due to thermalization and the resulting

---

[a] *Department of Physics & Astronomy, University of Oklahoma, Norman, OK 73019, USA. E-mail: Hadi.Afshari-1@ou.edu*
[b] *Department of Electrical Engineering, University at Buffalo, NY 14260, USA*
[c] *National Renewable Energy Laboratory, Golden, CO 80401, USA*
[d] *Swift Solar, San Carlos, CA, 94070, USA*

parasitic heat generation.[8,10] The second significant loss in solar cells is transmission loss, whereby photons with energies lower than the band gap pass through the device.[8] Both of these loss mechanisms can be somewhat reduced by using multijunction solar cell technology. However, the cost of this technology is currently prohibitive and therefore to date limits its use to only space photovoltaics (PV).[11,12]

The hot carrier solar cell (HCSC) has long been considered as a potential protocol to circumvent thermalization losses in single band gap solar cells and aims to harvest high energy electrons (holes) prior to excess energy dissipation.[13,14] Specifically, in semiconductors, excitation above the band gap results in high energy "hot" carriers (HCs) with a distribution temperature T_c (that forms *via* carrier–carrier interactions) far exceeding that of the lattice.[15–17] In most cases, the hot carrier population reaches a quasi-equilibrium state on a sub-picosecond time scale. Subsequently, slower carrier cooling ensues through predominantly carrier–phonon scattering, which is dominated by the emission of LO phonons in polar semiconductors – such as the metal halide perovskites studied here – until thermal equilibrium between the carriers and the lattice is reached.[13,16]

Hot carrier solar cell architectures aim to increase the intraband relaxation time of photogenerated carriers to values close to the carrier extraction time, such that carriers retain their kinetic energy upon collection.[18] Significantly, if achieved, such hot carrier solar cells promise power conversion efficiencies in excess of 60% for single junction solar cells.[14,15]

At present, there are two primary mechanisms for obtaining hot carrier solar cells that aim at slowing down non-equilibrium carrier cooling: (1) engineered quantum confinement accompanied by high illumination intensity in systems such as nanocrystals or multiple quantum well structures; (2) creating a phonon bottleneck in systems through high excitation densities using concentrated photoexcitation.[19–21] Note that both cases require high level illumination intensity. Fig. S1, which shows the room temperature power dependent TA results for the samples in this study, shows how the population of hot carriers increases dramatically with an increase in illumination power. In both scenarios, the cooling time may be extended to tens of picoseconds, influenced by the synergistic effects of the intrinsic phonon bottleneck, intensified Auger heating effects, and recently reported effects of valley scattering.[13,22–24]

While considerable work has been performed on traditional III–V materials,[25] recently there has also been growing interest in metal halide perovskites as potential systems for the realization of HCSCs with many recent studies suggesting the presence of long-lived hot carriers in these systems.[21,26–29] However, there is some debate in the community regarding the carrier thermalization pathways and the competing thermalization mechanisms.[15,27,30–32] Recently there has been evidence of hot carriers in perovskite device structures,[21,27,29] in addition to evidence of long hot carrier diffusion lengths in these materials,[33–35] providing encouragement for the potential of metal halide perovskites in hot carrier device applications.

Much of the early research in this field focused on hot carrier dynamics using ultrafast spectroscopy (using pulsed lasers), while solar cell devices operate in the CW or steady-state regime. Key innovations in the new cell architecture, which enabled high power pulsed and steady-state assessment of perovskites, have boosted their stability under both elevated temperatures and high-fluence photoexcitation, which are necessary to stimulate non-destructive hot carrier populations.[17,27,36]

While CW spectroscopy and time resolved techniques have traditionally been used to assess hot carriers in optical structures, here hot carrier effects and dynamics in metal halide perovskite solar cells in the ultrafast regime are assessed *in operando*. Specifically, the cooling dynamics of the hot carriers in triple halide perovskite ($FA_{0.8}Cs_{0.2}Pb_{1.02}I_{2.4}Br_{0.6}Cl_{0.02}$) solar cells are studied using power dependent (PD) transient absorption (TA) measurements under various biasing conditions including: (1) at V_{oc} open circuit with no current extraction, (2) at $V_{J_{sc}} = 0.02$ V, close to J_{sc} with maximum current passing through the solar cell and (3) at V_{max} or the maximum power point of these devices.

These data provide interesting insight into hot carrier dynamics in solar cells under practical operating conditions and the role that carrier absorption and extraction play in the formation and dissipation of hot carrier distributions in these systems. All these measurements were therefore performed using both front and back illumination, the orientation of which is described more fully below.

Materials and methods

The perovskite precursor chemicals were utilized in their original form and stored in a nitrogen glovebox. The preparation of perovskite solutions and the deposition of the film were carried out in the same nitrogen glovebox. Solutions for wide-gap perovskite precursors were created by dissolving formamidinium iodide (Greatcell), cesium iodide (Sigma-Aldrich), lead(II) iodide (TCI), lead(II) bromide, and lead(II) chloride (Alfa Aesar). This resulted in a 1.2 M solution of $FA_{0.8}Cs_{0.2}PbI_{2.4}Br_{0.6}Cl_{0.02}$ in DMF : DMSO, with a volumetric ratio of 3 : 1. It is important to note that the inclusion of a small amount of Cl is intentionally in stoichiometric excess.[36]

ITO-coated glass substrates from Thin Film Devices underwent an initial cleaning process involving sonication in acetone and propan-2-ol, followed by UV–ozone treatment for 10 minutes. Poly-TPD (poly(*N*,*N*′-bis-4-butylphenyl-*N*,*N*′-bisphenyl) benzidine) was applied through spin-coating from a 1 mg per mL solution in anhydrous chlorobenzene at 4000 rpm for 30 seconds. The solution was deposited dynamically and subsequently annealed at 110 °C for 10 minutes.[36]

PFN-Br (poly[(9,9-bis(3′-(*N*,*N*-dimethylamino)propyl)-2,7-fluorene)-*alt*-2,7-(9,9-dioctylfluorene)]) was utilized as a wetting layer, spin-coated from a 0.5 mg per mL solution in anhydrous methanol at 5000 rpm for 20 seconds. The solution was deposited dynamically. The perovskite film was then spin-coated at 5000 rpm for 60 seconds, with the solution spread on the substrate before spinning. Additionally, 120 μL of anhydrous methyl acetate was deposited onto the spinning wet film at 25 seconds into the spin cycle. The resulting film underwent annealing at 120 °C for 20 minutes.[36]

Following perovskite film deposition, a 1 nm layer of lithium fluoride was thermally evaporated at a rate of 0.1 Å s^{-1}. Subsequently, 30 nm of C_{60} (Lumtec) was thermally evaporated at a rate of 0.2 Å s^{-1} for the first 10 nm and 0.5 Å s^{-1} for the remaining 20 nm. A thin ALD nucleation layer of PEIE (polyethylenimine ethoxylated) was deposited through spin-coating a 0.025 wt% solution, prepared by diluting the purchased PEIE/water solution (40 wt%, Sigma-Aldrich), with anhydrous propan-2-ol. This layer was spin-coated at 5000 rpm for 20 seconds and deposited statically before spinning. The films were then annealed at 100 °C for 2 minutes.

Subsequently, 20 nm of SnO_x was deposited *via* ALD (Beneq TFS200 ALD), followed by 2 nm of zinc tin oxide (ZTO). An ITO electrode was deposited through room-temperature sputtering using a shadow mask (300 nm) in a Denton Explorer sputter tool. Finally, an oxide encapsulant layer was deposited *via* ALD, comprising 50 nm of Al_2O_3 interspersed with cycles of TiO_2.

The perovskite solar cells are measured using various characterizing techniques. The photovoltaic characteristics are examined through *J*–*V* measurements under the AM 1.5G solar spectrum, employing a Newport Oriel Sol2A solar simulator. A Keithley 2400 SourceMeter is employed to apply bias to the test cells and simultaneously measure the extracted current from the device.[36] Pump-probe transient absorption (TA) measurements were carried out at room temperature under various electrical bias conditions using a HELIOS TA spectrometer manufactured by Ultrafast Systems. The measurement employed a pump beam at 442 nm and 2 kHz of an Apollo-Y Optical Parametric Amplifier (OPA). The white light probe was generated in a sapphire crystal located inside the HELIOS spectrometer using the focused 1064 nm 2 kHz output of a Hyperion femtosecond amplified laser. The pulse duration of both the pump and the probe is approximately 350 fs.

Results and discussion

Fig. 1(a) shows a schematic of the energy band diagram of the solar cell assessed in this work. This architecture follows a typical perovskite solar cell comprising a heterostructure device, which consists of a poly-TPD hole transport layer (HTL) with C_{60} and SnO_2 electron transport layers (ETLs). These encapsulate a 400 nm halide perovskite absorber layer and the structure is completed with both upper and lower ITO layers to enable good device contact, while allowing for front and back transmission measurements. The "front side" of the device is the side through which solar irradiation typically impinges in these devices through the glass substrate and the subsequent HTL (see Fig. 1(a)). Based on this notation, the "back" of the

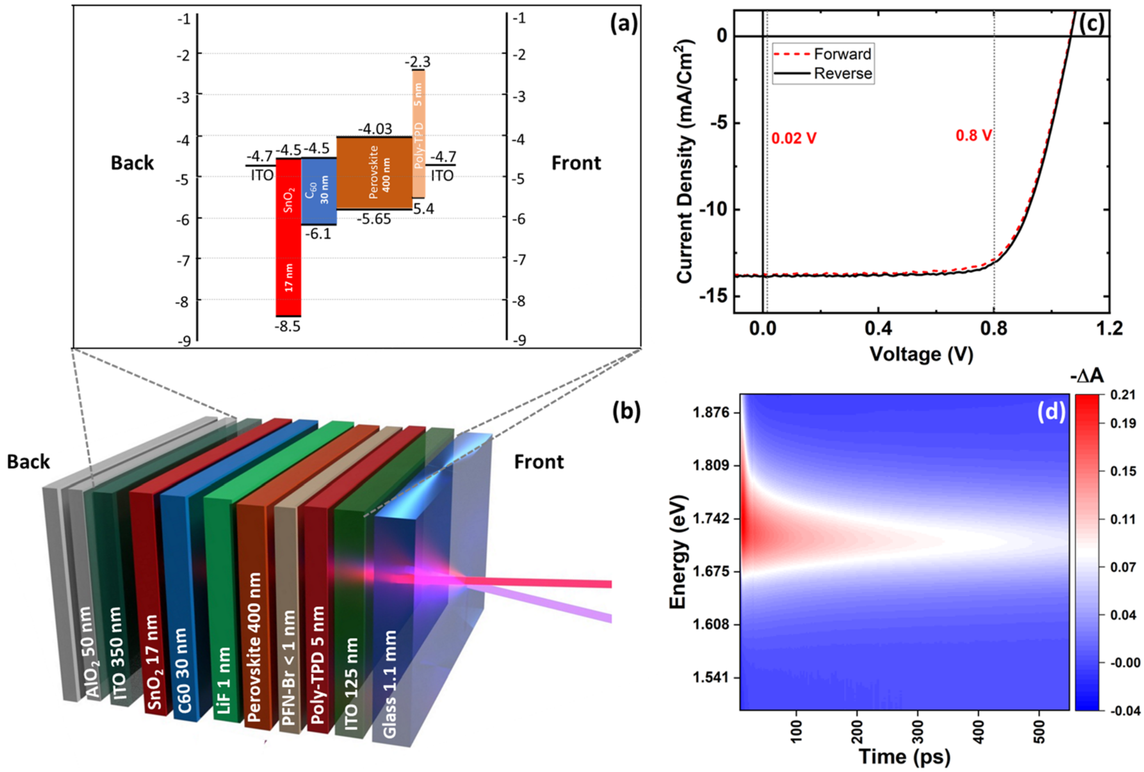

Fig. 1 (a) Schematic illustration of the band diagram of the metal halide perovskite solar cell under investigation. (b) Illustrative depiction of the structure of the solar cell indicating the front and back side orientation. (c) A comparison of the current density–voltage (*J*–*V*) response of the solar cell measured in forward (dashed red line) and reverse (solid black line) directions under 1 sun AM 1.5G. The vertical dashed lines indicate the voltages applied for the various TA measurements presented below. (d) Representative heat map of the transient (TA) at intermediate power at 300 K. The blue color indicates a small change in the absorption ($-\Delta A$) and red indicates a larger change in absorption ($-\Delta A$).

device therefore describes an orientation in which excitation occurs through the ITO covered SnO_2/C_{60} ETL.

Fig. 1(b) shows the full stack structure of the solar cell and illustrates the direction of the co-incident and overlapping pump (442 nm) and probe (white light visible range) beams under front side excitation (approx. 100 μm in diameter). The *k*-vector of the incident probe beam is perpendicular to the device layers, as also shown in Fig. 1(b).

Fig. 1(c) shows the light *J–V* graph of the solar cell taken under 1 sun AM1.5 conditions. The *J–V* measurement is performed in forward and reverse directions with negligible evidence of hysteresis, demonstrating the high quality of the device. While the J_{sc} of ~13 mA cm^{-2} reflects the non-optimum absorber thickness fabricated to facilitate absorption measurements, the quality of this device is evidenced by the high V_{oc} of ~1.1 V measured for these structures. The *J–V* response shown in Fig. 1(c) also indicates as vertical dashed lines the biases at which the power dependent TA (PD-TA) measurements were taken on this device. An additional TA measurement was also performed where the solar cell was not electrically contacted (true V_{oc}), and this condition is hereafter referred to as the "open circuit".

A representative TA heatmap (a color 2D plot of $-\Delta A$ *vs.* energy and time in picoseconds) is shown as an example in Fig. 1(d). This TA response exhibits the typical bleaching feature associated with interband absorption at the band gap energy with a high energy tail at early delay times, attributed to the presence of a high energy hot carrier population, enabling the investigation of hot carrier dynamics in these systems.[15,21,37]

In order to fully interpret the hot carrier dynamics in TA measurements, the role of recombination and its effect on temporal carrier population are critical. The upper panel of Fig. 2 describes the evolution of the non-equilibrium carrier distribution modeled using a standard Fermi gas formalism and the mechanisms that dissipate excess energy following the photoexcitation of carriers on a timescale spanning from femtoseconds to one second. Following photoexcitation, within a matter of several hundred femtoseconds, the initial carrier distribution, dictated by the energy and intensity of the pump, promptly undergoes elastic scattering *via* carrier–carrier interactions. This process leads to the establishment of a Fermi–Dirac distribution characterized by an extremely high non-equilibrium carrier temperature. Over the subsequent tens of picoseconds, the carriers experience inelastic scattering, effectively thermalizing the distribution.

The lower panel of Fig. 2 illustrates the effect of thermalization on the carrier distribution (calculated for the system studied here), over almost 2 orders of magnitude in the temporal window from sub-ps to tens of ps. Within the sub-picosecond regime (red region), elastic carrier–carrier scattering facilitates the redistribution of energy among photogenerated carriers as shown in the distribution labeled 0.4 ps. The photogenerated electrons (holes) rapidly attain a global non-equilibrium carrier distribution within the conduction (valence) band, known as hot carrier distribution, accompanied by a carrier temperature exceeding the lattice's equilibrium temperature ($t < 2$ ps). However, within a few tens of picoseconds post-light absorption (amber region, picoseconds range), carrier–phonon interactions dominate, leading to gradual thermalization of the carriers and the subsequent dissipation of excess energy and heat from the system in the 500 ps range.

Fig. 3(a) shows the evolution of the TA spectra with increasing pump-probe delay times, for the case of the non-contacted solar cell (V_{oc}) illuminated from the front side. Before providing a fuller discussion with respect to trends in the data and evolution of the photogenerated carriers, some points

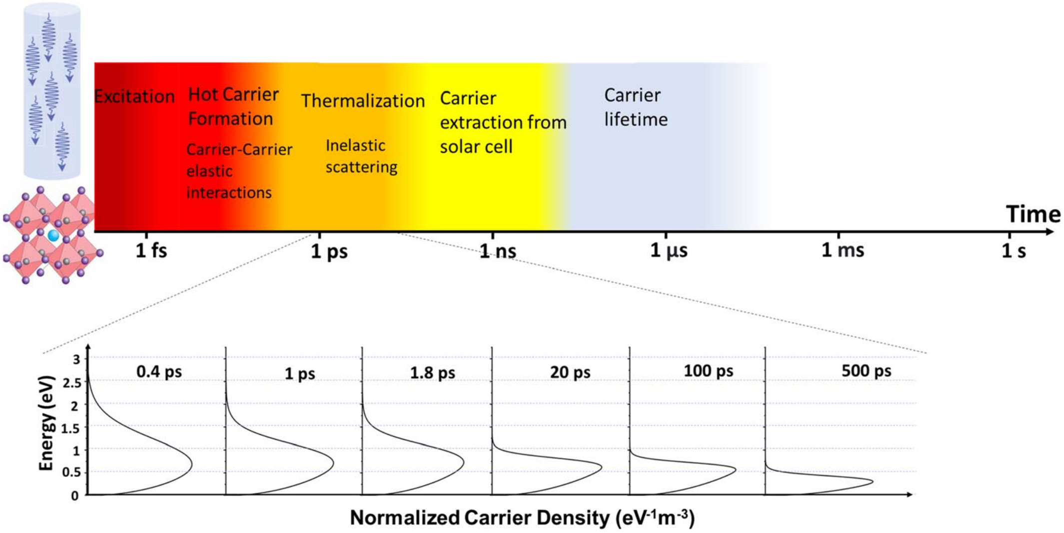

Fig. 2 The upper panel illustrates the sequence of processes of a semiconductor following photo-excitation, as depicted in the order shown. These include hot carrier formation within tens of femtoseconds, hot carrier thermalization over tens of picoseconds, carrier extraction from the solar cell occurring within a few to tens of nanoseconds, and carrier lifetimes that can extend up to microseconds. The lower panel focuses on the thermalization phase, showing the calculated carrier distribution for the studied system at various delay times. At 0.4 picoseconds, the data reveal the highest population of hot carriers, with longer delay times corresponding to a reduced population of these carriers.

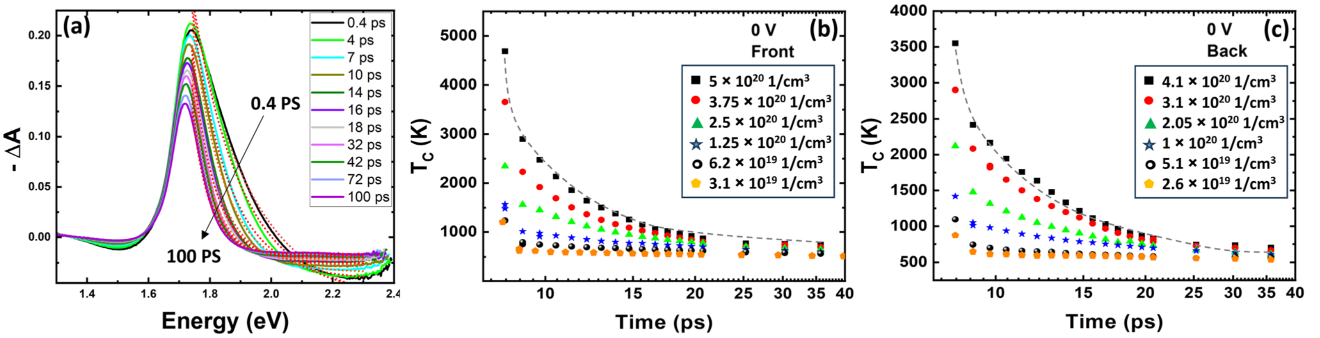

Fig. 3 (a) Transient absorption of the solar cell excited from the front side of the structure. The red dotted lines represent the fitting of the high energy side of the curves with a generalized form of Planck's radiation law, eqn (1). The extracted carrier temperatures, T_c, for front (b) and back side (c) illumination, respectively.

regarding these measurements need to be made: (1) the same experiment is performed with various powers, external biases, and from both front and back sides of the solar cells (the results for other biases and conditions are presented in the SI, Fig. S2). (2) Since a very high-power pulsed laser beam is used, it is crucial to have a control protocol to assess the performance of the cells after each round of TA measurements. Current density–voltage (*J*–*V*) measurements are performed after each round of TA experiments for this purpose. The results of these experiments are presented in Fig. S3. As Fig. S3 indicates, there is not a noticeable change in the performance of the cells after TA experiments, indicating that high power TA measurements have not affected the cells meaningfully. (3) Table 1 shows the pulse peak power densities used for the TA measurements and associated carrier densities generated in the solar cell through front and back side illumination. For the same powers used for front and back side illumination, the generated carrier density is different due to the difference in absorption of the HTL and ETL as will be discussed in more detail shortly.

While individual pulse peak power density values are extremely high, the highest average power density is approximately equivalent to 815 times the Sun's intensity at the surface of the Earth, which is within the typical range in concentrated solar systems that are appropriate platforms for the application of hot carrier solar cells.[38–40] The latest generation ultrafast laser system described in the Materials section of this paper enables us to access higher carrier concentrations without excessively heating the sample. The temporal separation between the pulses (500 µs) is usually much longer than the thermalization of the hot carriers while the overall duration of pulses is extremely short (350 fs). This allows the carriers to cool down before the next pulse arrives, preventing overheating of the sample and enabling studies under such extreme excitation levels, vital for hot carrier physics. Femtosecond laser systems remain the only way to investigate the hot carrier dynamics at extremely high excitation levels without the downside of damaging the solar cells.

Table 1 Pulse power densities used for the TA measurements and their associated carrier densities generated within the perovskite absorber layer for front side and back side illumination

	Carrier density	
Pulse power density	Frontside	Backside
12×10^{10} W cm^{-2}	5×10^{20} cm^{-3}	4.1×10^{20} cm^{-3}
9×10^{10} W cm^{-2}	3.75×10^{20} cm^{-3}	3.1×10^{20} cm^{-3}
6×10^{10} W cm^{-2}	2.5×10^{20} cm^{-3}	2.05×10^{20} cm^{-3}
3×10^{10} W cm^{-2}	1.25×10^{20} cm^{-3}	1×10^{20} cm^{-3}
1.5×10^{10} W cm^{-2}	6.25×10^{19} cm^{-3}	5.1×10^{19} cm^{-3}
0.7×10^{10} W cm^{-2}	3.1×10^{19} cm^{-3}	2.6×10^{19} cm^{-3}

According to Fig. 3(a), spectra recorded at early delay times exhibit a high energy tail associated with the distribution of hot carriers.[41–43] At long delay times, the photobleach experiences a redshift and linewidth (*Γ*) narrowing associated with hot carrier thermalization and carrier cooling to the band edge.[43,44] It is worth mentioning that in some materials the photobleach behavior is opposite in terms of the full width at half maximum (FWHM), reporting broadening of *Γ* for longer delay times.[21] Upon photoexcitation, the Burstein–Moss effect (which reflects state filling due to the high rate of carrier generation) competes with band gap renormalization (which is associated with coulombic repulsion due to the high density of photogenerated carriers), which induces a competing redshift.

In addition to the dynamics related to the band gap bleach, photo-induced absorption (PIA) is also evident in the TA on both sides of the main photobleach peak Fig. 3(a). While below band gap PIA is explained through (probe-induced) excitation of photogenerated (pump-induced) carriers, above-band gap PIA has also previously been ascribed to the change in the imaginary part of the refractive index in metal halide perovskites, which serves to modulate the optical response of these materials.[15,44,45]

On inspection, the TA shown in Fig. 3(a) shows that up to ∼6 ps, the magnitude of photobleaching increases, while the FWHM of the TA narrows (TA curves focused in this time window are depicted in SI, Fig. S4). This pattern qualitatively follows the Fermi–Dirac distribution of the electrons in the conduction band (holes in the valence band) illustrated in Fig. 2 after excitation, which is explained by the relaxation of hot carriers to lower energy levels in the conduction band. At increasing delay times, $t > 6$ ps, the magnitude of the bleach systematically decreases due to a combination of radiative recombination and lateral redistribution of the carriers towards regions outside of the probe beam zone. Also, the presence of built-in fields at both interfaces (HTL and ETL) of the absorber layer, which extend towards the center of the metal halide perovskite layer, causes drifting of carriers towards the transport layers. This reduces the carrier density (n_0) in the absorber, which can lower the magnitude of the bleach. The reduction in the carrier density is accounted for when plotting the hot carrier distribution at longer time delays up to 500 ps in the lower panel of Fig. 2.

As seen in Fig. 3(a), while the low energy side of the TA curves is relatively unchanged (except for the reduction of the PIA at longer delay times) with time, the high energy side changes dramatically. These changes reflect the temporal evolution and thermalization of the photogenerated hot carrier distribution. The carrier temperature, T_c, can be extracted from the high energy side of the TA curves using the Fermi–Dirac distribution function, which, under hot carrier conditions ($(E - E_F) \gg k_B T_c$), is approximated using the Maxwell–Boltzmann distribution, yielding[15,21]

$$-\Delta A(\hbar\omega) = -A_0(\hbar\omega)\exp\left(-\frac{\hbar\omega - E_F}{k_B T_c}\right) \tag{1}$$

Or alternatively one can use the relation

$$\frac{\Delta T}{T}(E) \propto \exp\left(-\frac{E - E_F}{k_B T_c}\right) \tag{2}$$

where E_F is the quasi-Fermi level, k_B is the Boltzmann constant, and T_c is the hot carrier temperature. This is a technique developed by the HC community to evaluate HC dynamics and temperature across several systems.[15,21,46–48] Here, simple "tail fitting" is used to perform a qualitative assessment of high energy carrier relaxation/dynamics as well as the role of bias and/or excitation geometry. Examples of the "fits" used to determine T_c from eqn (2) are shown as red dotted lines in Fig. 3(a) for the device under non-contact bias-free front side illumination.

Fig. 3(b) and (c) show the laser fluence (power/carrier density) dependence of T_c extracted from a non-contacted (V_{oc}) device illuminated through the front side glass substrate (see Fig. 1(a)) and also back side illumination (SI, Fig. S5 shows the same data for cases $V_{J_{sc}}$ and V_{max}). Within the femtosecond time frame (red section in Fig. 2) after photoexcitation, the photogenerated carriers form a high temperature hot carrier distribution. Over tens to hundreds of femtoseconds, elastic carrier–carrier interactions dominate, resulting in non-equilibrium carrier temperatures, T_c, as high as 5000 K, in this case. As shown in Fig. 3(b) and (c), higher T_c values are achieved for higher power densities. For example, for a carrier density of 3.1×10^{19} cm^{-3} (a pulse peak power density of 0.7×10^{10} W cm^{-2}), T_c reaches ~1000 K, while for a carrier density of 5×10^{20} cm^{-3} (12×10^{10} W cm^{-2}), the temperature is >4000 K. The power independent regimes evident in these data at $t > 10$–20 ps are considered the equilibrium regime, where the carriers are thermalized and are nearly at the lattice temperature.

When considering the direction of excitation, illumination through the glass substrate and subsequent HTLs (denoted "front") results in higher T_c, as compared to the illumination through the "back" (bc) and ETLs. Specifically, T_c at 0.4 ps for the highest pulse power density of 12×10^{10} W cm^{-2} is ~4700 K for front side (fr) excitation and ~3600 K for back side illumination. The main reason for this difference in hot carrier temperature is the higher carrier densities generated within the perovskite absorber layer in the case of front side illumination, as presented in Table 1.

Although understanding the non-uniform T_c with respect to excitation direction requires further investigation, the non-uniform carrier temperatures suggest a subtle interplay between carrier absorption and extraction/transfer in these architectures. Under front side illumination, more photons are absorbed within the active perovskite layer (with respect to back side illumination through C_{60}/SnO_2) due to the relatively thin wide gap poly-TPD layer that comprises the HTL, which that absorbs little of the incident light under direct excitation (see Fig. S6). The larger relative absorption under front side illumination increases the generated carrier density within the perovskite directly, as presented in Table 1, in the MHP layer, leading to an increase in both the hot carrier temperature and the relative phonon bottleneck that would be generated.

As is illustrated in Fig. 1(a), incident light on the back side initially traverses and is absorbed in a relatively thicker electron transport layer comprising C_{60} and SnO_2. C_{60}, in particular, has a high absorption coefficient in the visible range (~1.8 eV, direct band gap), which will inevitably result in approximately 20% fewer 442 nm photons from the pump beam reaching the halide perovskite layer under back side excitation, when compared to illumination of the device through the front side (thinner poly-TPD). The relative absorption through these two geometries is illustrated in Fig. S6, which shows a transfer matrix simulation of the structures under front and back side illumination, with the lower photon transmission at the back. It is therefore postulated that the difference in T_c observed in Fig. 3(b) and (c) reflects the difference in photogenerated carriers in the perovskite film under the two excitation conditions, which is lower under back side illumination (with respect to the front) reducing also the relative phonon bottleneck – which is highly carrier density dependent – and therefore T_c induced under excitation from the back (relative to front excitation).

However, here it must also be noted that the T_c extracted from the TA reflects the average temperature of the carriers, comprising both hot electron and hot hole thermalization; as such, little is known directly regarding the relative temperature and thermalization of these constituent carriers. It is additionally postulated that the relative carrier transport and extraction efficiency affect the "average" carrier temperature and that depending upon excitation orientation, the respective thermalization rates of electrons and holes are different. This is discussed further below.

In Fig. 3(b) and (c), irrespective of the relative carrier temperature, T_c systematically reduces in both excitation orientations to a temperature approaching that of the lattice (equilibrium), a process mediated by carrier–carrier and carrier–phonon scattering such that the photogenerated carrier population equilibrates with the thermal reservoir.

In addition to the data presented in Fig. 3(b) and (c) at V_{oc}, T_c was also extracted under bias at 0.02 V – $V_{J_{sc}}$ and 0.8 V – V_{max} (see Fig. S5) as deduced from the J–V response under ambient conditions at 1 sun AM 1.5G illumination (see Fig. 1(c)).

Fig. 4 compares the carrier temperatures at (a) the earliest delay time, 0.4 ps, and (b) after thermalization is mostly complete, 100 ps, for different powers and biases ((1) V_{oc}, not contacted, (2) $V_{J_{sc}} = 0.02$ V, and (3) $V_{max} = 0.8$ V) under front side illumination. The error bars in this figure are our estimated uncertainties of the fitting procedure of ΔA curves (see Fig. 3(a)). The fitting procedure includes two cases: one where the fitting window covers most of the high-energy side and extends close to the peak of the photo-bleach curve, and another where the window similarly spans the high-energy side and extends toward the tail. The error bars represent the difference between these two fitting approaches. For an in-depth explanation of these two approaches, refer to ref. 21. As shown in Fig. 4(a), the carrier temperature is lowest under J_{sc} biasing conditions across all power levels for a delay time of 0.4 ps. This is expected, as the maximum current flows through the solar cell under J_{sc} conditions, influencing the density of states and the availability of states for hot carrier thermalization.[49] Additionally, the increased system dynamics enhance the likelihood of interactions, in favor of inelastic processes.

Interestingly, in Fig. 4(a), in the initial fast decay regime (0.4 ps), there appears a power dependent increase in the carrier thermalization at V_{max}, with minor exceptions. In this temporal regime, carrier cooling is dominated by Frohlich interactions and cooling *via* carrier–LO phonon interactions.[10,15,50] At V_{max}, the carrier transport through the absorber is dominated by diffuse currents that are strongly coupled to the lattice *via* the polar nature of these systems. The power dependence of the carrier temperature is also seen for the 100 ps data at V_{max} (see Fig. 4(b)). At V_{max}, the built-in field actively exerts force on photogenerated carriers and there is I_{max} current through the solar cell. Apparently, the combination of a non-zero internal electric field and current transfer specifically at high carrier densities (high powers) under V_{max} conditions impacts the carrier distribution, promoting carrier–carrier interactions that lead to higher carrier temperatures (unlike the J_{sc} case). This is in accordance with the BGR effect (intensified under V_{max} conditions) in halide perovskites, which dominates at early time delays before the hot carriers start to thermalize.

There are two intertwined effects that perhaps are also playing a role. First, metal halide perovskites are known to be poor thermal conductors[51] and the role acoustic phonons play in the dissipation of heat, as well as enabling the creation of a hot phonon bath,[52–54] should not be overlooked. Recently, studies on III–V quantum well structures have also shown that the addition of acoustic phonons to theoretical modeling allows for a more complete model to explain the observed hot carrier behavior.[55] Second, the influence of polarons, which are known to contribute considerably to the optoelectronic properties of metal halide perovskites,[56–58] has also been suggested to result in hot carrier stabilization *via* hot phonon reabsorption;[43] however, this stabilization would have to coincide with the formation process of the polarons rather than after they are fully formed.

The carrier cooling time (thermalization rate) is extracted from full biexponential fits to the temporal evolution of carrier temperature responses (see Fig. 3(b) and (c)) with the extracted parameters τ_1 and τ_2 describing intra-band relaxation – thermalization – of the carriers at open circuit and the dissipation of excess heat in the system, respectively; for data under the other various biases, see the SI (Fig. S5). A comparison of cooling times τ_1 and τ_2 – the temporal decays – under various bias conditions at higher excitation powers is presented in Fig. 5. It is observed that for higher pulse powers, namely 9×10^{10} W cm^{-2} and 12×10^{10} W cm^{-2}, τ_1 and τ_2 have a bias dependence, while for the low powers, this behavior is not apparent. Fig. 5(a) and (c) show the relative cooling time at shorter times ($t < 5$ ps) at 12×10^{10} W cm^{-2} and 9×10^{10} W cm^{-2}, respectively; Fig. 5(b) and (d) show the behavior at $t > \sim 10$ ps, also for the two respective pulse powers discussed.

The fast and slower heat dissipation regimes observed here have been reported previously in metal halide perovskites and

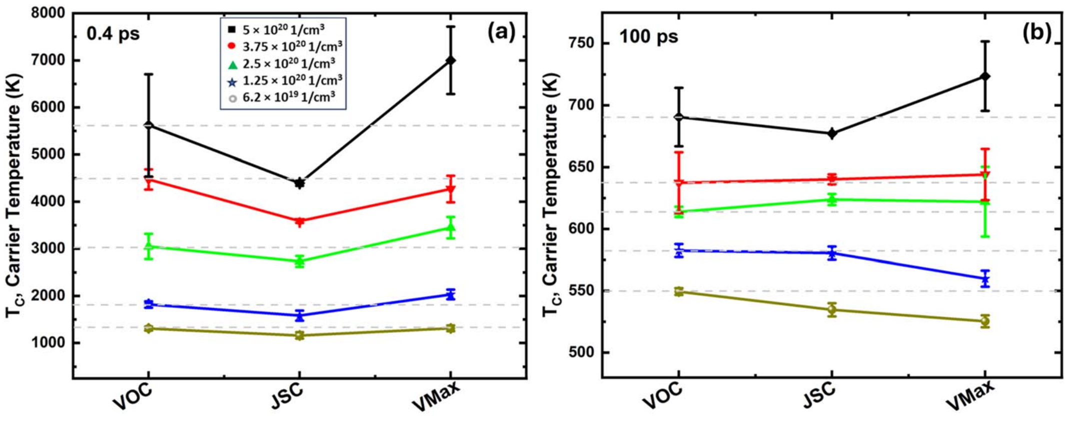

Fig. 4 (a) Carrier temperatures at 0.4 ps for all the laser pump powers as a function of external bias. (b) Carrier temperatures at 100 ps for all the powers of the front side illumination as a function of external bias. Illumination is incident from the front side for both (a) and (b).

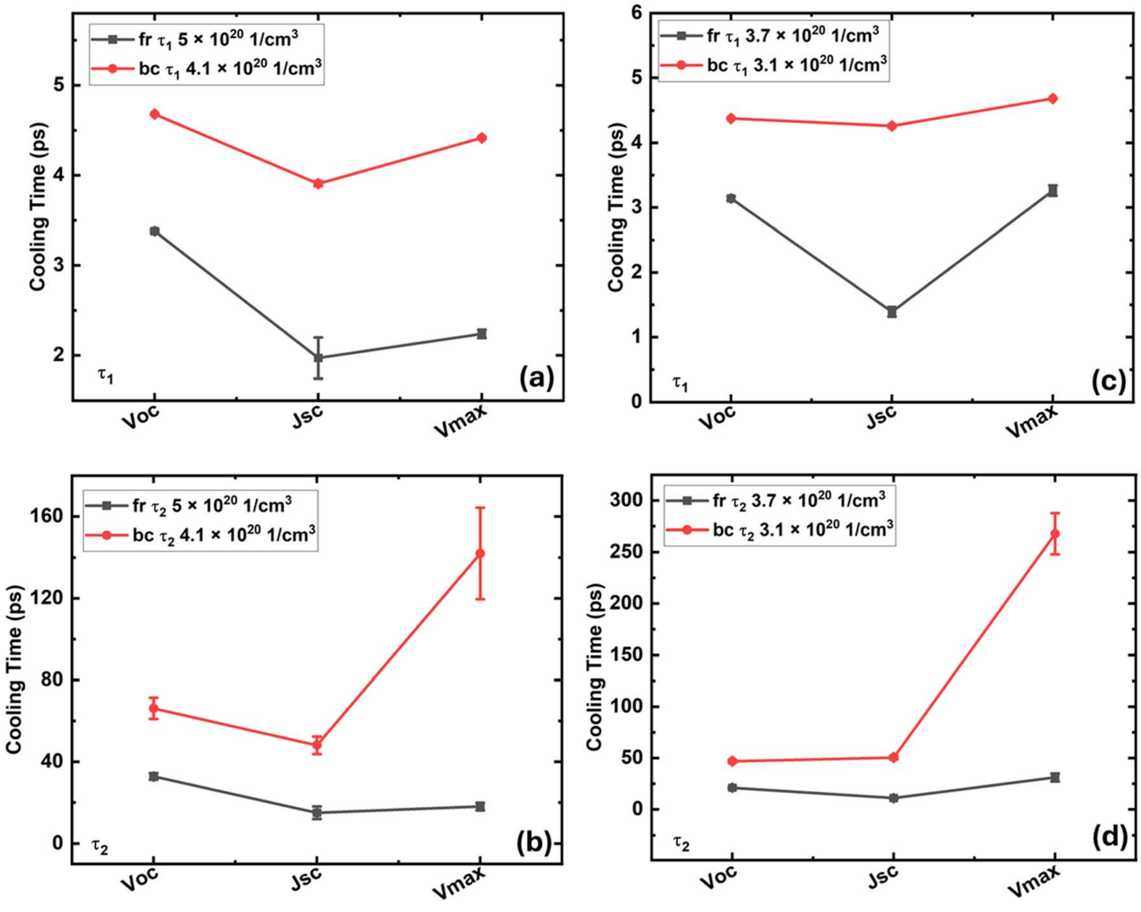

Fig. 5 Extracted cooling times at pulse power densities of 9×10^{10} W cm^{-2} and 12×10^{10} W cm^{-2} for both front and back side illumination, measured under various bias conditions. A short cooling time (τ_1) in the range of 3–5 ps and a longer cooling time (τ_2) in the range of 10–250 ps are extracted from the fitting of carrier temperature *vs.* time responses. (a) and (b) The results for τ_1 and τ_2 at 12×10^{10} W cm^{-2} and (c) and (d) the results for τ_1 and τ_2 at 9×10^{10} W cm^{-2}. In all cases, the black squares represent front side illumination results and the red circles represent back side illumination results.

have been attributed to a combination of phonon bottleneck effects and Auger re-heating effects, at moderate to high carrier densities.[15,21,37,41] More recently, it has also been suggested that the slower cooling regime observed across metal halide perovskites is due to simple lattice heating and their low thermal conductivity, in general;[27,59] that is, only the fast component of the decay curves relates to the hot carrier dynamics and LO phonon-mediated thermalization in these systems.

Remarkably, in Fig. 5 it is evident in all cases that the thermalization time is faster under front side illumination (black symbols – *via* thin poly-TPD) as compared to back illumination (red symbols – *via* C_{60}-ETL). The error bars in this figure are due to the results of two fitting windows. One fitting window covers up to 1 ns and the second window reaches the highest time delay available for that measurement (our TA system's delay time limitation is 7 ns). Indeed, despite the relatively cooler T_c and reduced carrier generation in the perovskite absorber layer with respect to front side illumination (see Fig. 3(b) and (c)), the carrier lifetime under back side illumination is longer under all bias conditions (closed red circles – Fig. 5). This may be due in part to hot carriers photogenerated within the C_{60} ETL, which help sustain the longer-lived hot carrier population observed during back side illumination.

Here, the initial decay time (τ_1) is on the order of 1–5 ps (Fig. 5(a and c)), while the second, longer decay (τ_2) occurs over tens of ps (10–300 ps) – Fig. 5(b and d). Previous reports indicate an enhanced relaxation time with increasing power density specifically for (τ_1) consistent with the creation of a hot phonon bottleneck.[13,15,60] In all cases (with one minor exception), the cooling times are the lowest for the J_{sc} conditions, similar to carrier temperatures at earlier times (0.4 ps). This reflects the effect of the dynamic carrier transport under J_{sc} conditions on hot carrier lifetime. It therefore appears that carrier thermalization is modulated by carrier extraction (driven by external biasing).

This behavior further supports the relative role of the phonon bottleneck in inhibiting carrier thermalization in these systems. That is, when photogenerated carriers are rapidly removed from the solar cell under – for example – short circuit conditions, the thermalization rate decreases and the carrier dependent phonon bottleneck is reduced. If the photogenerated carriers are retained within the device – at open circuit –

the relative carrier density is higher, leading to a larger phonon bottleneck that reduces the relative carrier thermalization.

When considering back side illumination through the ETL (closed red circles – Fig. 5), the behavior is somewhat different than that of front side excitation (*via* HTL), but consistent with earlier work assessing TA measurements of individual HTL/perovskite and ETL/perovskite sub-stacks of the samples studied here, which also showed non-equivalent carrier dynamics in the system.[61] Under back side illumination, the photogenerated electrons travel farther than the holes prior to collection, while the case is reversed under front side illumination.

Once again, the T_c extracted from the TA (Fig. 1(d)) reflects the average temperature of the carriers, comprising both electron and hole carrier thermalization; as such, little is known directly regarding the relative temperature and thermalization of these constituent carriers. It is postulated that the collection of the photogenerated carriers at the back side of the structure is less efficient than that of the front side photogenerated carriers and that this increases the relative thermalization rate of hot carriers under back side illumination, despite the lower relative carrier density generated in the absorber under this excitation orientation (Fig. 3(b) and (c)). While further work is required to support this hypothesis, it is consistent with the data presented and earlier work that shows parasitic barriers in similar metal perovskite solar cells at the perovskite/SnO_2–C_{60} interface that require an efficient electron tunneling and thermionic emission rate to operate efficiently and are exacerbated at lower temperature.[27,62,63]

Conclusion

In this study, it is shown that the behavior of photogenerated hot carriers in metal halide perovskite solar cells differs significantly when comparing their dynamics in non-contacted devices at open circuit, V_{oc}, to those observed when the cells operate under short circuit conditions, $V_{J_{sc}}$, or at the maximum power point, V_{max}. This is attributed to the relative contribution of carrier density, the role of field aided or diffuse transport and/or collection and the respective role of these properties in the creation of a carrier–LO phonon bottleneck particularly in the sub-ps regime, where strong carrier–phonon dynamics are at play. Notably, despite the relatively cooler T_c and reduced carrier generation in the perovskite absorber layer with respect to front side illumination, the carrier lifetime under back side illumination is longer under all bias conditions.

Conflicts of interest

The authors declare no conflict of interest.

Data availability

Data for this article, including power and bias dependent TA and *J*–*V* results, are available in Hot Carrier Dynamics in Operational Metal Halide Perovskite Solar Cells and **https://zenodo.org/records/16513826**.

The supplementary information document contains: a power dependent TA graph to show the effect of higher powers on hot carrier population and temperature. The fittings of the TA curves for V_{OC}, J_{SC} and V_{MAX} conditions. Control current density–voltage (*J*–*V*) measurement results. An example of TA data focused on sub 7 ps. Data representing hot carrier temperature *versus* time for the J_{SC} and V_{MAX} conditions. The layer absorbance profile of the solar cells from two sides based on simulations in Setfos software, which utilizes transfer matrix formalism. See DOI: **https://doi.org/10.1039/d5el00063g**.

Acknowledgements

Support from the Department of Energy EPSCoR Program and the Office of Basic Energy Sciences, Materials Science, and Energy Division under award DE-SC0019384 is acknowledged. IRS and VRW also acknowledge support from the Center for Advanced Semiconductor Technologies (CAST) at the University of Buffalo. VM and HA are grateful for the support received from the Dodge Family postdoctoral fellowship program at the University of Oklahoma. This material is based in part upon work supported by the National Science Foundation under Grant No. OISE-2230706. This work was authored in part by the National Renewable Energy Laboratory, operated by the Alliance for Sustainable Energy, LLC, for the U.S. Department of Energy (DOE) under Contract No. DE-AC36-08GO28308. The views expressed in the article do not necessarily represent the views of the DOE or the U.S. Government.

References

1 D. Lincot, The new paradigm of photovoltaics: from powering satellites to powering humanity, *C. R. Phys.*, 2017, **18**(7–8), 381–390.
2 L. M. Fraas and L. D. Partain, *Solar Cells and Their Applications*, John Wiley & Sons, 2010.
3 C. Toledo and A. Scognamiglio, Agrivoltaic systems design and assessment: a critical review, and a descriptive model towards a sustainable landscape vision (three-dimensional agrivoltaic patterns), *Sustainability*, 2021, **13**(12), 6871.
4 M. Trommsdorff, *et al.*, Combining food and energy production: design of an agrivoltaic system applied in arable and vegetable farming in Germany, *Renew. Sustain. Energy Rev.*, 2021, **140**, 110694.
5 D. P. Birnie III, Analysis of energy capture by vehicle solar roofs in conjunction with workplace plug-in charging, *Sol. Energy*, 2016, **125**, 219–226.
6 F. Mohammadi, Design, analysis, and electrification of a solar-powered electric vehicle, *J. Sol. Energy Res.*, 2018, **3**(4), 293–299.
7 Y. Miyamoto, *et al.*, *Development of 2nd-Generation Solar Charging System and Generating Performance in the USA*, SAE Technical Paper, 2023.
8 L. C. Hirst and N. J. Ekins-Daukes, Fundamental losses in solar cells, *Prog. Photovoltaics: Res. Appl.*, 2011, **19**(3), 286–293.

9 T. Kirchartz and U. Rau, What makes a good solar cell?, *Adv. Energy Mater.*, 2018, **8**(28), 1703385.

10 Y. Zhang, *et al.*, A review on thermalization mechanisms and prospect absorber materials for the hot carrier solar cells, *Sol. Energy Mater. Sol. Cells*, 2021, **225**, 111073.

11 M. Yamaguchi, *et al.*, Multi-junction solar cells paving the way for super high-efficiency, *J. Appl. Phys.*, 2021, **129**(24), 240901.

12 F. Dimroth and S. Kurtz, High-efficiency multijunction solar cells, *MRS Bull.*, 2007, **32**(3), 230–235.

13 H. Esmaielpour, *et al.*, Exploiting intervalley scattering to harness hot carriers in III–V solar cells, *Nat. Energy*, 2020, **5**(4), 336–343.

14 D. K. Ferry, V. R. Whiteside and I. R. Sellers, Pathways to hot carrier solar cells, *J. Photon. Energy*, 2022, **12**(2), 022204.

15 Y. Yang, *et al.*, Observation of a hot-phonon bottleneck in lead-iodide perovskites, *Nat. Photonics*, 2016, **10**(1), 53–59.

16 W. Lin, *et al.*, Carrier Cooling in Lead Halide Perovskites: A Perspective on Hot Carrier Solar Cells, *ACS Energy Lett.*, 2023, **9**(1), 298–307.

17 S. Kahmann and M. A. Loi, Hot carrier solar cells and the potential of perovskites for breaking the Shockley–Queisser limit, *J. Mater. Chem. C*, 2019, **7**(9), 2471–2486.

18 H. Esmaielpour, *Type-II Quantum Well Hot Carrier Solar Cells*, 2018.

19 H. Esmaielpour, *et al.*, Strong Dimensional and Structural Dependencies of Hot Carrier Effects in InGaAs Nanowires: Implications for Photovoltaic Solar Cells, *ACS Appl. Nano Mater.*, 2024, **7**, 2817–2824.

20 H. Baker, *et al.*, Breaking phonon bottlenecks through efficient auger processes in perovskite nanocrystals, *ACS Nano*, 2023, **17**(4), 3913–3920.

21 J. W. M. Lim, *et al.*, Hot carriers in halide perovskites: How hot truly?, *J. Phys. Chem. Lett.*, 2020, **11**(7), 2743–2750.

22 H. Esmaielpour, *et al.*, Tailoring hot carrier effects in semiconductor nanowires by spatial confinement, in *Physics, Simulation, and Photonic Engineering of Photovoltaic Devices XIII*, SPIE, 2024.

23 H. Esmaielpour, *et al.*, Influence of Auger heating and Shockley-Read-Hall recombination on hot-carrier dynamics in InGaAs nanowires, *Phys. Rev. B*, 2024, **109**(23), 235303.

24 T. Wang, *et al.*, Protecting hot carriers by tuning hybrid perovskite structures with alkali cations, *Sci. Adv.*, 2020, **6**(43), eabb1336.

25 G. Conibeer, *et al.*, Hot carrier solar cell absorber prerequisites and candidate material systems, *Sol. Energy Mater. Sol. Cells*, 2015, **135**, 124–129.

26 G. Xing, *et al.*, Long-range balanced electron-and hole-transport lengths in organic-inorganic CH3NH3PbI3, *Science*, 2013, **342**(6156), 344–347.

27 S. Sourabh, *et al.*, Evidence of hot carrier extraction in metal halide perovskite solar cells, *Prog. Photovoltaics: Res. Appl.*, 2024, **32**, 546–555.

28 L. J. van de Ven, *et al.*, Cation Influence on Hot-Carrier Relaxation in Tin Triiodide Perovskite Thin Films, *ACS Energy Lett.*, 2024, **9**, 992–999.

29 S. Gong, *et al.*, A hot carrier perovskite solar cell with efficiency exceeding 27% enabled by ultrafast hot hole transfer with phthalocyanine derivatives, *Energy Environ. Sci.*, 2024, **17**(14), 5080–5090.

30 B. T. Diroll and R. D. Schaller, Intraband cooling in all-inorganic and hybrid organic–inorganic perovskite nanocrystals, *Adv. Funct. Mater.*, 2019, **29**(37), 1901725.

31 A. Mondal, *et al.*, Ultrafast exciton many-body interactions and hot-phonon bottleneck in colloidal cesium lead halide perovskite nanocrystals, *Phys. Rev. B*, 2018, **98**(11), 115418.

32 H.-H. Fang, *et al.*, Long-lived hot-carrier light emission and large blue shift in formamidinium tin triiodide perovskites, *Nat. Commun.*, 2018, **9**(1), 243.

33 H. J. Jöbsis, *et al.*, The Effect of Charge Carrier Cooling on the Ultrafast Carrier Dynamics in Cs2AgBiBr6 Thin Films, *ACS Energy Lett.*, 2025, **10**, 1050–1056.

34 M. Monti, *et al.*, Hot carriers in mixed Pb-Sn halide perovskite semiconductors cool slowly while retaining their electrical mobility, *Phys. Rev. B*, 2020, **102**(24), 245204.

35 Z. Guo, *et al.*, Long-range hot-carrier transport in hybrid perovskites visualized by ultrafast microscopy, *Science*, 2017, **356**(6333), 59–62.

36 H. Afshari, *et al.*, FACsPb Triple Halide Perovskite Solar Cells with Thermal Operation over 200 °C, *ACS Energy Lett.*, 2023, **8**(5), 2408–2413.

37 J. Fu, *et al.*, Hot carrier cooling mechanisms in halide perovskites, *Nat. Commun.*, 2017, **8**(1), 1–9.

38 Y. Xing, *et al.*, A review of concentrator silicon solar cells, *Renew. Sustain. Energy Rev.*, 2015, **51**, 1697–1708.

39 A. W. Bett, *et al.*, 30% monolithic tandem concentrator solar cells for concentrations exceeding 1000 suns, in *Conference Record of the Twenty-Eighth IEEE Photovoltaic Specialists Conference-2000 (Cat. No. 00CH37036)*, IEEE, 2000.

40 B. L. Sater and N. D. Sater, High voltage silicon VMJ solar cells for up to 1000 suns intensities, in *Conference Record of the Twenty-Ninth IEEE Photovoltaic Specialists Conference, 2002*, IEEE, 2002.

41 K. K. Chauhan, *et al.*, Hot phonon and auger heating mediated slow intraband carrier relaxation in mixed halide perovskite, *IEEE J. Quantum Electron.*, 2020, **57**(1), 1–8.

42 C. V. Franco, *et al.*, Charge Carrier Relaxation in Colloidal FAPbI3 Nanostructures Using Global Analysis, *Nanomaterials*, 2020, **10**(10), 1897.

43 J. Yang, *et al.*, Acoustic-optical phonon up-conversion and hot-phonon bottleneck in lead-halide perovskites, *Nat. Commun.*, 2017, **8**(1), 14120.

44 J. Yin, *et al.*, Manipulation of hot carrier cooling dynamics in two-dimensional Dion–Jacobson hybrid perovskites via Rashba band splitting, *Nat. Commun.*, 2021, **12**(1), 3995.

45 M. B. Price, *et al.*, Hot-carrier cooling and photoinduced refractive index changes in organic–inorganic lead halide perovskites, *Nat. Commun.*, 2015, **6**(1), 8420.

46 I. Baranowski, *et al.*, Monte Carlo simulation of ultrafast carrier relaxation in type I and type II InAs-based quantum wells, in *Physics, Simulation, and Photonic Engineering of Photovoltaic Devices XII*, SPIE, 2023.

47 M. Giteau, *et al.*, Identification of surface and volume hot-carrier thermalization mechanisms in ultrathin GaAs layers, *J. Appl. Phys.*, 2020, **128**(19), 193102.

48 A. Le Bris, *et al.*, Hot carrier solar cells: controlling thermalization in ultrathin devices, *IEEE J. Photovoltaics*, 2012, **2**(4), 506–511.

49 E. K. Tekelenburg, *et al.*, Mechanism of Hot-Carrier Photoluminescence in Sn-Based Perovskites, *Adv. Mater.*, 2025, **37**(5), 2411892.

50 S. Sourabh, *et al.*, Hot carrier redistribution, electron-phonon interaction, and their role in carrier relaxation in thin film metal-halide perovskites, *Phys. Rev. Mater.*, 2021, **5**(9), 095402.

51 N. Onoda-Yamamuro, T. Matsuo and H. Suga, Calorimetric and IR spectroscopic studies of phase transitions in methylammonium trihalogenoplumbates (II), *J. Phys. Chem. Solids*, 1990, **51**(12), 1383–1395.

52 A. Pisoni, *et al.*, Ultra-Low Thermal Conductivity in Organic–Inorganic Hybrid Perovskite CH3NH3PbI3, *J. Phys. Chem. Lett.*, 2014, **5**(14), 2488–2492.

53 R. Heiderhoff, *et al.*, Thermal Conductivity of Methylammonium Lead Halide Perovskite Single Crystals and Thin Films: A Comparative Study, *J. Phys. Chem. C*, 2017, **121**(51), 28306–28311.

54 T. Ye, *et al.*, Ultra-high Seebeck coefficient and low thermal conductivity of a centimeter-sized perovskite single crystal acquired by a modified fast growth method, *J. Mater. Chem. C*, 2017, **5**(5), 1255–1260.

55 D. V. Izak Baranowski, I. R. Sellers and S. M. Goodnick, Hot Phonon Bottlenecks and the Role of Non-Equilibrium Acoustic Phonons in III-V Multi-Quantum Well Systems, *arxiv*, 2025, preprint, arXiv:2507.06455v1, DOI: 10.48550/arXiv.2507.06455.

56 M. B. Johnston and L. M. Herz, Hybrid perovskites for photovoltaics: charge-carrier recombination, diffusion, and radiative efficiencies, *Acc. Chem. Res.*, 2016, **49**(1), 146–154.

57 A. Furasova, *et al.*, Nanophotonics for perovskite solar cells, *Adv. Photonics Res.*, 2022, **3**(9), 2100326.

58 H. Esmaielpour, *et al.*, Role of Exciton Binding Energy on LO Phonon Broadening and Polaron Formation in (BA) 2PbI4 Ruddlesden–Popper Films, *J. Phys. Chem. C*, 2020, **124**(17), 9496–9505.

59 S. Sourabh, *et al.*, *Abstract: F63.00008 : Hot Carrier Dynamics in Bulk and 2D Perovskites*, Bulletin of the American Physical Society, 2020, **65**(1).

60 Y. Zhang, *et al.*, Review of the mechanisms for the phonon bottleneck effect in III–V semiconductors and their application for efficient hot carrier solar cells, *Prog. Photovoltaics: Res. Appl.*, 2022, **30**(6), 581–596.

61 B. Rebecca Scheidt, G. E. Wieliczka, I. R. Sellers, J. Luther and M. C. Beard, *Exploring the Effects of Dimensionality and In situ Solar Cell Behavior on Hot Carriers in Lead Halide Perovskites*, MRS Spring Meeting, 2022.

62 C. Brown, *et al.*, Potential of high-stability perovskite solar cells for low-intensity–low-temperature (LILT) outer planetary space missions, *ACS Appl. Energy Mater.*, 2018, **2**(1), 814–821.

63 H. Afshari, *et al.*, Temperature-Dependent Carrier Extraction and the Effects of Excitons on Emission and Photovoltaic Performance in Cs0. 05FA0. 79MA0. 16Pb (I0. 83Br0. 17) 3 Solar Cells, *ACS Appl. Mater. Interfaces*, 2022, **14**(39), 44358–44366.